

An entropic bottleneck, dynamical gating, and outward redistribution of roaming in a designed Chesnavich-type model

Stephen Wiggins

Hetao Institute of Mathematics and Interdisciplinary Sciences, Shenzhen, China
School of Mathematics, University of Bristol, Bristol BS8 1TW, United Kingdom

July 8, 2026

Abstract

Roaming reactions are organized not by potential-energy saddles but by transition states that are unstable invariant objects in phase space, periodic orbits in the two degrees of freedom studied here. To ask what controls roaming, we modify the Chesnavich model of a barrierless ion–molecule dissociation: its orientation-dependent angular hindrance is replaced by a transverse-stiffness ridge whose angular frequency peaks at an interior radius, and the classical dynamics are studied at a fixed energy just above the dissociation threshold. Comparing two ensembles that differ only in this angular interaction (same radial channel, energy, and inward initial conditions) isolates its effect. The ridge gates entry into the inner well, cutting inner capture from 57% to 15% and returning most of the incoming flux directly to reactants; it does not eliminate roaming but relocates it outward, suppressing it inside the ridge and switching it on farther out. The model retains analogues of the original model’s three transition states (tight, free-rotor, and outer orbiting orbits), which we locate as unstable periodic orbits. The tight orbit spans a dividing surface that coincides, within numerical accuracy, with the variational minimum-flux surface, and it carries no barrier along the reaction coordinate: a deep entropic bottleneck placed at an interior radius by the stiffness maximum. Its entropic character is shared with the original model. Strength-matched monotone controls show that the gating tracks the hindrance strength at the bottleneck radius; what the interior maximum supplies is placement, concentrating that strength where it gates most effectively. The trajectories it admits roam nonstatistically, with nonexponential gap-time distributions: the entropic bottleneck governs how much is captured, not the dynamics that follow.

1 Introduction

Roaming and entropic transition states. Conventional transition-state theory places a locally nonrecrossing dividing surface at a rank-one saddle of the potential energy surface. Two kinds of process fall outside that picture: barrierless bond fissions, whose transition states must be found variationally because the potential rises monotonically along the reaction coordinate, and roaming reactions, in which a partially dissociated fragment executes large-amplitude motion in a flat long-range region and then reacts or escapes without following the minimum-energy path. Since H-atom roaming was identified in formaldehyde [1] it has been documented across many systems and is now recognized as a general feature of gas-phase dynamics [2, 3, 4, 5, 6]. For barrierless association and dissociation the controlling loose transition state is located variationally [11, 10], and its cost is predominantly entropic rather than tied to a saddle. A related but distinct line of work concerns

the “entropic intermediate” of nonstatistical organic dynamics, a free-energy minimum on a flat region of the surface with long residence times and heavy recrossing [7]; we treat it here as an adjacent phenomenon rather than the same physics. In phase space these transition states are not saddles but unstable invariant objects and the dividing surfaces attached to them: periodic orbits in systems with two degrees of freedom, and normally hyperbolic invariant manifolds in general [19, 18, 17]. The model studied here has two degrees of freedom, so its transition states are periodic orbits, and roaming is organized by a small set of them.

Entropy barriers. That a rate can be controlled by entropy rather than energy is long established: Zhou and Zwanzig [8] gave a solvable model in which diffusion through a channel of varying width produces a purely entropic barrier. Most relevant here, Makarov [9] showed that a localized maximum of a transverse frequency along a reaction coordinate generates an entirely entropic free-energy barrier, one with no potential maximum along the coordinate, because the constrained free energy

$$F(x) = V(x) + k_B T \ln \frac{\omega_{\perp}(x)}{\omega_0} \quad (1)$$

acquires a maximum wherever the transverse mode stiffens, even where $V(x)$ is flat. Here x is the reaction coordinate, $V(x)$ the potential along it, $\omega_{\perp}(x)$ the transverse-mode frequency at x , ω_0 a reference frequency, and $k_B T$ the thermal energy. In the model studied here the reaction coordinate is the radial separation r and the transverse mode is the angular coordinate θ . Makarov further showed that such a barrier is dynamically distinct from what controls crossing times: transition-path-time statistics can be insensitive to a barrier that nonetheless dominates the free-energy profile. Both points recur below. The entropic character of such a bottleneck is not itself new: in a barrierless system any variational bottleneck is entropic, and the Chesnavich model we build on already has one. What we add is a deliberately deep entropic bottleneck, placed at an interior radius by an interior maximum of the transverse stiffness, embedded in a Hamiltonian model of roaming where its dynamical consequences can be followed.

The Chesnavich model and the question. Chesnavich introduced a model Hamiltonian for ion–molecule dissociation to study competition between multiple transition states [20, 21]; its planar, zero-angular-momentum form is now a standard laboratory for roaming. Mauguière, Collins, Ezra, Farantos and Wiggins analyzed roaming in it in phase space, identifying the tight and orbiting transition states with dividing surfaces attached to unstable periodic orbits and associating roaming with free-rotor orbits born in saddle–center bifurcations [22, 23, 24, 25, 26]; Krajňák and Waalkens, and Krajňák and Wiggins, mapped these structures in detail and across parameter space [27, 28, 29, 30, 31, 32]. In that model the tight and orbiting transition states are tied respectively to the orientation-locking angular hindrance and to the centrifugal barrier. We ask a dynamical question. If the orientation-locking hindrance is replaced, on the same barrierless radial channel, by a ridge in the transverse stiffness (an interior maximum of the angular frequency, with no potential barrier along the channel), how is roaming changed? At fixed energy, and for the same incoming ensemble, does the ridge promote roaming, suppress it, or reorganize it? Our central finding is the last: the ridge gates entry into the inner well, admitting only a small fraction of the incoming flux and returning most of it directly to reactants, and it does not increase the roaming fraction but displaces it outward, suppressing it inside the ridge and switching it on farther out.

Three transition states. The phase-space account of this behavior rests on three transition states, all unstable periodic orbits located here at fixed energy: a tight orbit, a free-rotor orbit,

and an outer orbiting orbit. The tight orbit gates entry to the well; the dividing surface it spans coincides with the variational minimum-flux surface (as verified in Sec. 8 by comparing the tight-orbit action with the fixed-radius minimum flux) and carries no potential barrier along the radial coordinate, so it is a purely entropic bottleneck, made deep and placed at an interior radius by the transverse-stiffness maximum. The free-rotor orbit sorts direct from roaming trajectories; the orbiting orbit gates escape to products. The tight orbit is the one the ridge reshapes: its entropic character it shares with the Chesnavich tight transition state, but the designed ridge makes it deep enough to control capture. The roaming it admits is nonstatistical, with nonexponential gap-time distributions: the entropic bottleneck sets how much is captured, not the fate of what follows.

Organization. Section 2 fixes the classical Chesnavich model. Section 3 introduces the designed transverse-stiffness model. Section 4 presents the central result: two trajectory ensembles compared under identical conditions (same radial potential, energy, and incoming ensemble), differing only in the angular interaction, so that any difference in outcome is attributable to that term alone. Sections 5, 6, and 7 locate the three transition states, and Sec. 8 relates the tight entropic bottleneck to Makarov’s picture. Section 9 concludes; computational methods and the gap-time analysis are in Appendices A and B.

2 The classical Chesnavich model

With zero overall angular momentum and planar geometry, Chesnavich’s two-degree-of-freedom (2-DoF) Hamiltonian is [20, 22, 30]

$$H = \frac{p_r^2}{2\mu} + \frac{p_\theta^2}{2} \left(\frac{1}{I_{\text{CH}_3}} + \frac{1}{\mu r^2} \right) + V(r, \theta), \quad (2)$$

where r is the distance from the CH_3^+ center of mass to the H atom and θ the relative orientation. The potential is a barrierless radial channel plus an orientation-dependent term that hinders free rotation of the fragment, favoring the aligned geometry $\theta = 0$ and switching off with distance:

$$V(r, \theta) = V_{\text{CH}}(r) + \frac{1}{2}V_0(r)[1 - \cos 2\theta], \quad V_0(r) = V_e e^{-\alpha(r-r_e)^2}, \quad (3)$$

$$V_{\text{CH}}(r) = \frac{D_e}{c_1 - 6} \left\{ 2(3 - c_2)e^{c_1(1-x)} - (4c_2 - c_1c_2 + c_1)x^{-6} - (c_1 - 6)c_2 x^{-4} \right\}, \quad (4)$$

with $x = r/r_e$. As r decreases and $V_0(r)$ grows, this term stiffens and confines the fragment near alignment; we call it the *orientation lock* (or Chesnavich lock) for brevity. The parameters, phenomenological rather than fitted to data, are $D_e = 47$ kcal/mol, $r_e = 1.1$ Å, $c_1 = 7.37$, $c_2 = 1.61$, $V_e = 55$ kcal/mol, $I_{\text{CH}_3} = 2.3734$ u Å², $\mu = 0.9445$ u, and $\alpha = 1$ Å⁻² [20, 22]; the x^{-4} term is the ion-induced-dipole $-1/r^4$ tail.

The transition states of this surface, which has two degrees of freedom, are periodic orbits, not saddles. As established by Mauguière, Collins, Ezra, Farantos and Wiggins and by Krajňák and Waalkens, the orbits that organize roaming are unstable periodic orbits on a fixed energy shell, none located at a critical point of $V(r, \theta)$: an inner orientation-locking (tight) orbit whose *periodic-orbit dividing surface* (PODS), the dividing surface spanned by an unstable periodic orbit, gates entry to the well; an outer relative-equilibrium orbit on the centrifugal barrier of the effective radial potential $V_{\text{CH}}(r) + \frac{1}{2}p_\theta^2(1/I_{\text{CH}_3} + 1/\mu r^2)$ (the orbiting, or loose, transition state) whose PODS gates passage to the radical channel; and an intermediate free-rotor family whose PODS is used to separate direct from roaming trajectories [22, 27, 28].

A single quantity captures how tightly the orientation lock—the *angular potential* $\frac{1}{2}V_0(r)[1 - \cos 2\theta]$ —confines the fragment at each radius: the *harmonic transverse frequency*. The transverse degree of freedom is the angular coordinate θ , transverse to the radial reaction coordinate r , and near the aligned geometry $\theta = 0$ it behaves like a vibration. Expanding the angular potential about $\theta = 0$ gives $\frac{1}{2}V_0(r)[1 - \cos 2\theta] \simeq V_0(r)\theta^2$, a harmonic well whose *curvature*—the second derivative in θ , that is, the angular force constant—is $2V_0(r)$. The matching kinetic term in Eq. (2) is $\frac{1}{2}(1/I_{\text{CH}_3} + 1/\mu r^2)p_\theta^2$, so the effective angular mass is $(1/I_{\text{CH}_3} + 1/\mu r^2)^{-1}$. A harmonic oscillator has frequency $\sqrt{\text{force constant/mass}}$, which here is

$$\Omega_{\text{Ch}}(r) = \sqrt{2V_0(r)\left(\frac{1}{I_{\text{CH}_3}} + \frac{1}{\mu r^2}\right)}. \quad (5)$$

It is a local measure of orientational stiffness: the larger it is, the more sharply the fragment is held near alignment. Why a large transverse frequency should impede the reaction even where the radial potential is flat is the mechanism we build the next section around; here we note only its shape. Since $V_0(r) = V_e e^{-\alpha(r-r_e)^2}$ falls off monotonically for $r > r_e$, so does $\Omega_{\text{Ch}}(r)$, which might suggest that the channel has no interior flux minimum. It does have one. The harmonic frequency omits both the r -dependence of the available channel energy and the anharmonicity of the hindered rotor, and the exact radial-surface flux computed in Sec. 5 has a genuine, if shallow, interior minimum on the Chesnavich surface. The Chesnavich model therefore does possess an entropic bottleneck; it is shallow, and arises mainly from the radial variation of channel energy together with the angular dynamics rather than from a maximum of transverse stiffness.

3 The designed transverse-stiffness model

We keep the kinetic energy of the Chesnavich model unchanged (the same reduced mass, moment of inertia, and r -dependent angular mass $a(r)$) and keep its long-range attraction (the ion-induced-dipole $-1/r^4$ tail), but replace the orientation lock by a localized transverse-stiffness ridge that we *design*, that is, construct by hand to have a prescribed property rather than fit to a real molecule: a single interior maximum of the transverse stiffness. The transverse stiffness is the strength of the angular restoring force, measured by the harmonic transverse frequency $\Omega(r)$; a stiffer transverse mode (larger Ω) confines the angular motion more tightly. The designed Hamiltonian is

$$H = \frac{p_r^2}{2\mu} + \frac{1}{2}a(r)p_\theta^2 + V_{\text{rad}}(r) + \frac{1}{2}B(r)[1 - \cos 2\theta], \quad a(r) = \frac{1}{I_{\text{CH}_3}} + \frac{1}{\mu r^2}, \quad (6)$$

in which the angular potential's prefactor $B(r)$ —its strength as a function of r —is a localized Gaussian bump centered at an interior radius r_c ,

$$B(r) = \frac{1}{2}a(r)^{-1}\Omega_0^2 e^{-(r-r_c)^2/2\sigma^2}. \quad (7)$$

By the small-oscillation argument of Sec. 2, now with the ridge amplitude $B(r)$ in place of the lock amplitude $V_0(r)$ and $a(r)$ the kinetic coefficient of Eq. (6), the harmonic transverse frequency about $\theta = 0$ is

$$\Omega(r) = \sqrt{2B(r)a(r)} = \Omega_0 e^{-(r-r_c)^2/2\sigma^2}. \quad (8)$$

The factor $a(r)^{-1}$ in $B(r)$ is chosen precisely to cancel the r -dependence of the angular mass, so that $\Omega(r)$ is an exact Gaussian with a single smooth interior maximum at $r = r_c$ (Fig. 1c), in contrast to the monotone $\Omega_{\text{Ch}}(r)$ of the Chesnavich lock.

Why an interior maximum of $\Omega(r)$ acts as a bottleneck is Makarov’s observation [9], Eq. (1), restated here for the angular mode. The angular motion is fast compared with the radial approach, so at each r it completes many oscillations while r barely changes, and one may remove it by averaging. Removing a degree of freedom in equilibrium statistical mechanics means replacing it by its partition function—a sum over the states it can occupy—and paying a free-energy cost $-k_B T \ln(\text{that sum})$. For a harmonic mode of frequency $\Omega(r)$ the classical transverse partition function, over θ and p_θ together, is $Z_\perp(r) = k_B T / \hbar \Omega(r)$, so the free energy along r becomes

$$G(r) = V_{\text{rad}}(r) - k_B T \ln Z_\perp(r) = V_{\text{rad}}(r) + k_B T \ln \Omega(r) + \text{const}, \quad (9)$$

which is Eq. (1) with the angular coordinate playing the role of the transverse mode (the constant absorbs the reference frequency ω_0). The added term is entropic, not energetic: Ω enters only through Z_\perp , the number of accessible angular states, and not through the energy of any configuration. A stiffer angular spring (larger Ω) holds the fragment in a narrower cone about alignment, so fewer orientations are accessible; fewer accessible states mean lower entropy and therefore higher free energy. At fixed energy the same statement reads: the number of transverse states below a transverse energy E_\perp scales as E_\perp / Ω , so a stiffer mode has fewer of them [9, 11]. Wherever $\Omega(r)$ is largest, $G(r)$ is highest.

The lock and the ridge run through the *same* frequency formula, $\Omega = \sqrt{2A(r)a(r)}$, differing only in the angular amplitude $A(r)$: $A = V_0(r)$ for the Chesnavich lock and $A = B(r)$ for the designed ridge. For the lock $V_0(r)$ falls off monotonically, so Ω_{Ch} and its free-energy term $k_B T \ln \Omega_{\text{Ch}}$ decrease monotonically with r : by this mechanism alone the lock cannot place a bottleneck in the interior. For the ridge $\Omega(r)$ peaks at r_c [Eq. (8)], so $k_B T \ln \Omega$ peaks there too—an entropic bottleneck placed in the interior by design, even though $V_{\text{rad}}(r)$ has no barrier there. This is Makarov’s transverse-stiffening mechanism built into the angular coordinate of a roaming model. The price is a larger angular amplitude: $B(r)$ reaches ~ 156 kcal/mol at r_c , against ~ 16 kcal/mol for $V_0(r_c)$ (Fig. 1b).

This canonical $k_B T \ln \Omega$ is a heuristic: we work at fixed energy, not in a thermal bath, so the quantity we actually compute is its microcanonical counterpart, the exact transverse flux through a surface at radius R , whose interior minimum plays the role of the free-energy maximum (Sec. 5). The contrast with the lock is one of mechanism, not of outcome: the Chesnavich model does still have a shallow interior bottleneck, but—as Sec. 5 shows—it comes chiefly from the way the energy available to the angular mode varies with r , together with the full hindered-rotor dynamics, not from a maximum of transverse stiffness. Our ridge places the bottleneck directly, through the stiffness itself.

For the radial channel we use either the Chesnavich $V_{\text{CH}}(r)$ or a Lennard-Jones LJ(8,4) form, both decaying as $-1/r^4$ at long range,

$$V_{\text{LJ}}(r) = D_e \left[(r_e/r)^8 - 2(r_e/r)^4 \right]. \quad (10)$$

We use the near-identity of the results under this substitution (Sec. 4) to establish that the gating is produced by the angular ridge and is insensitive to the shape of the barrierless radial channel: with the long-range tail and the angular term held fixed, replacing $V_{\text{CH}}(r)$ by $V_{\text{LJ}}(r)$ leaves the inner-capture drop essentially unchanged. The ridge itself is radially localized at r_c ; what the substitution rules out is a dependence on the detailed shape of the radial channel potential, not radial structure as such. The model parameters are listed in Table 1.

Table 1: Parameters of the designed model, Eqs. (6)–(10). The “sharp ridge” values are used throughout unless stated otherwise. Energies in kcal/mol, lengths in Å, masses in u.

quantity	symbol	value
reduced mass	μ	0.9445
CH ₃ moment of inertia	I_{CH_3}	2.3734
well depth / tail scale	D_e, r_e	47, 1.1
Chesnavich shape constants	c_1, c_2	7.37, 1.61
Chesnavich lock height / width	V_e, α	55, 1
ridge peak frequency squared	Ω_0^2	200
ridge center / width	r_c, σ	2.2, 0.5
roaming energy	E	2

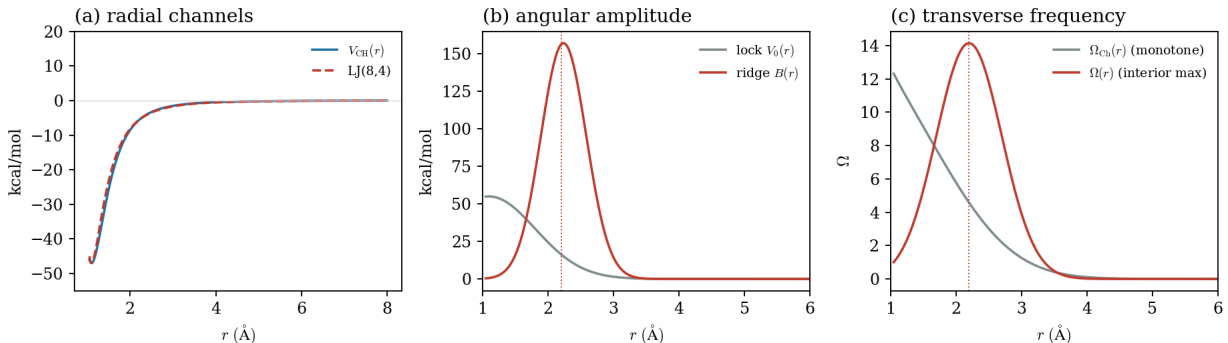


Figure 1: Construction of the designed model. (a) The two barrierless radial channels, $V_{\text{CH}}(r)$ and the LJ(8,4) form; neither has a radial barrier along the approach, and both decay as $-1/r^4$ at long range. (b) Angular hindrance amplitude versus r : the monotone Chesnavich lock $V_0(r)$ ($\alpha = 1$) and the entropic ridge $B(r)$, taller and concentrated near $r_c = 2.2$ Å. (c) Harmonic transverse frequency: $\Omega_{\text{CH}}(r)$ decreases monotonically, whereas the designed $\Omega(r)$ has a single interior maximum at r_c .

4 The entropic ridge gates inner capture and displaces roaming outward

The model was built to ask a dynamical question, and we answer it first, before locating the phase-space structures that explain the answer. The question is what the localized entropic ridge does to roaming *relative to* the orientation-locking interaction of the original Chesnavich surface. We answer it with a controlled comparison in which everything but the angular interaction is held fixed. We fix the radial channel at the Chesnavich potential $V_{\text{CH}}(r)$, fix the energy $E = 2$, and fix the incoming fixed-energy ensemble; the only difference between the two runs is the angular term, the Chesnavich lock $\frac{1}{2}V_0(r)[1 - \cos 2\theta]$ in one and the entropic ridge $\frac{1}{2}B(r)[1 - \cos 2\theta]$ in the other. The ensemble is a 240×240 grid in $(\theta_0, p_{\theta,0})$ launched inward from $r_0 = 6$ Å at fixed E , with the inward radial momentum fixed by the energy constraint and energetically inaccessible launch points removed; a trajectory is counted as reaching the well if it crosses $r < 1.6$ Å, and the integrator and ensemble are documented in Appendix A. This is the dynamical counterpart of the matched control at the level of the flux (Sec. 5), where the same ridge is placed on $V_{\text{CH}}(r)$ at the level of the exact directional flux; here we compare its trajectory consequences against the lock at fixed radial energetics.

What changes. Figure 2 reports the comparison, and two effects are large and unambiguous. First, the ridge *gates entry into the inner well*: entry into the well ($r < 1.6 \text{ \AA}$) falls from 57.3% under the monotone lock to 14.7% under the ridge, and the fraction of the ensemble returned directly to the outer region without entering the well rises correspondingly from 37.4% to 80.3% (Fig. 2a). The mechanism is visible in the penetration profile (Fig. 2c): the monotone lock funnels incoming trajectories toward $\theta = 0$ and into the well, so the cumulative penetration $P(r_{\min} < r)$ rises steadily; the ridge instead reflects all but a narrow channel near $\theta = 0$, and $P(r_{\min} < r)$ is gated sharply just outside r_c . Second, the ridge *does not increase the roaming fraction*; it *displaces the roaming fraction outward*, where the roaming fraction counts trajectories that cross the classifier radius three or more times, in either direction, before reacting or escaping. At the classifier radius $r_{\text{class}} = 3.5 \text{ \AA}$ the roaming (nonreactive) fraction is essentially unchanged, 5.3% \rightarrow 4.9%. But the radial profile of the statistic changes qualitatively (Fig. 2b): under the monotone lock repeated crossings are already present at smaller radii and decay quickly outward; under the ridge they are suppressed inside r_c , switch on sharply just beyond it, and persist to larger radii, exceeding the lock’s curve at every radius beyond $\sim 3.8 \text{ \AA}$. The two runs agree closely when the LJ(8,4) channel is substituted for $V_{\text{CH}}(r)$ (inner capture 57.3%/15.1%, within 1%), confirming that the effect is carried by the angular interaction and not by the radial form.

What this is, and what it is not. The result carries four qualifications. (i) *“Reactive” means entry into the well, not committed product.* A trajectory is counted as reactive if its closest approach reaches $r < 1.6 \text{ \AA}$. The flow is volume-preserving and the well is not an attractor, so this denotes entry into the molecular well, not a committed product yield: a captured trajectory may recross and redissociate. The gating result is a statement about inner-well capture (Appendix A), and the same definition is used for the classifier ensemble of Sec. 7. (ii) *Amplitude and localization, separated by a control.* The two angular interactions differ in *amplitude* as well as in radial profile: the ridge reaches $\sim 156 \text{ kcal/mol}$ at r_c , against $\sim 16 \text{ kcal/mol}$ for the lock at the same radius. To separate the two effects we ran strength-matched monotone controls: the same lock form $V_e e^{-(r-r_e)^2}$ with V_e raised, on the same channel and ensemble. Capture falls monotonically with the hindrance strength at the bottleneck radius, $V_0(r_c)$: raising it from the standard 16.4 to 46.5, 80, and 156 kcal/mol gives capture 57.3%, 33.0%, 24.9%, and 17.8%. The r_c -matched monotone lock ($V_0(r_c) = 156$, requiring $V_e = 523$) also displaces roaming outward much as the ridge does (switching on near 3.8 \AA), and its capture transfers between radial channels (17.8% on both V_{CH} and LJ). Both headline effects therefore follow from strong orientational hindrance in the region of the bottleneck radius and are not unique to an interior maximum. What the interior maximum supplies is placement and economy: it concentrates the hindrance at the gating radius, so the ridge gates far more effectively than a monotone profile of equal global peak strength (14.7% against 33.0%) and does so without imposing a very large hindrance at all smaller radii; the residual difference between the ridge and the r_c -matched control (14.7% against 17.8%) is the contribution of the localized profile itself. (iii) *The roaming fraction is parameter-dependent; the redistribution is not.* The roaming fraction is sensitive to the Chesnavich switching parameter α . For the early-switching lock ($\alpha = 4$), whose hindrance has all but vanished by $r \simeq 2 \text{ \AA}$, almost the entire incoming ensemble is captured ($\sim 99.9\%$) and the baseline roaming fraction is tiny ($\sim 0.2\%$); against that baseline the ridge both reduces capture and *increases* the measured roaming fraction. It would therefore be misleading to speak of “the” roaming fraction of the Chesnavich model. The robust result, common to $\alpha = 1$ and $\alpha = 4$, is the inner-well gating; the outward redistribution is demonstrated explicitly for the $\alpha = 1$ comparison through the full classifier-radius sweep of Fig. 2b, while the raw roaming percentage at any single classifier radius changes strongly with α . (iv) *This is conditional-on-entry intermediate dynamics.*

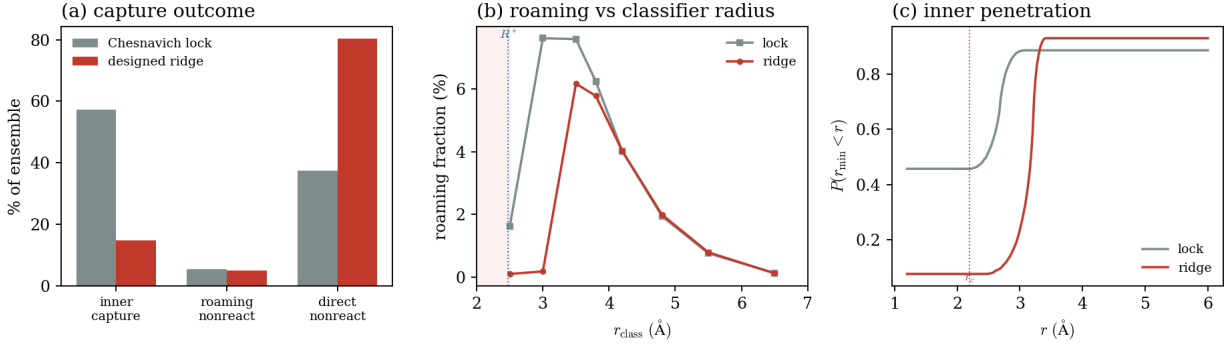


Figure 2: The controlled comparison at $E = 2$. The radial channel $V_{\text{CH}}(r)$, the energy, and the inward fixed-energy ensemble are identical in the two runs; only the angular term differs, set to the Chesnavich lock (the orientation-locking term of the original model) in one and to the entropic ridge (the localized transverse-stiffness maximum at r_c) in the other. (a) Inner-capture outcome: the ensemble partitioned into inner capture (entry to $r < 1.6$ Å), roaming nonreactive, and direct nonreactive. The ridge cuts inner capture from 57.3% to 14.7% and raises direct nonreactive return from 37.4% to 80.3%, while the roaming (nonreactive) fraction is nearly unchanged (5.3% \rightarrow 4.9%). (b) The roaming fraction versus classifier radius: under the ridge it is suppressed inside r_c , switches on beyond it, and persists farther out than under the lock, crossing above the lock’s curve beyond ~ 3.8 Å. The variational bottleneck $r^* = 2.47$ Å for this channel is marked. (c) Cumulative inner penetration $P(r_{\min} < r)$: the lock funnels trajectories into the well; the ridge gates them just outside r_c .

The launch surface $r_0 = 6$ Å lies *inside* the outer orbiting transition state ($r_{\text{OTS}} \simeq 7.48$ Å, Sec. 6); this is a comparison of intermediate-region dynamics conditional on inward entry, not a complete reactant-to-product scattering calculation.

The remaining sections locate the phase-space structures that explain this behavior: a variational flux bottleneck just outside the ridge, an invariant dynamical transition state far outside it, and a classifier between the two that tracks neither.

5 The variational flux bottleneck

The statistical bottleneck is the dividing surface spanned by the tight orbit. For a radial dividing surface $r = R$ at energy E , the exact fixed-energy directional flux is [19]

$$\Phi_R(E) = \oint_0^{2\pi} 2\sqrt{\frac{2[\varepsilon(R) - U_{\text{ang}}(R, \theta)]_+}{a(R)}} d\theta, \quad \varepsilon(R) = E - V_{\text{rad}}(R), \quad (11)$$

with $U_{\text{ang}}(R, \theta) = \frac{1}{2}B(R)[1 - \cos 2\theta]$ and $[\cdot]_+$ the positive part; $\Phi_R(E)$ is the area of the transverse (angular) phase space (θ, p_θ) , on the energy shell at $r = R$, that is energetically able to cross outward. The variational bottleneck r^* minimizes $\Phi_R(E)$ over R [11, 13, 14]; we work at fixed energy throughout, and r^* is the fixed-energy analogue of the maximum of the canonical constrained free energy of Eq. (1), which is why we describe it as entropic. We also define the angular confinement factor

$$C(R, E) = \frac{\Phi_R(E)}{\Phi_R^{\text{free}}(E)}, \quad \Phi_R^{\text{free}}(E) = 2\pi \cdot 2\sqrt{2\varepsilon(R)/a(R)}, \quad (12)$$

the fraction of the free-rotor transverse phase space that remains accessible; normalizing a hindered quantity by its free-rotor value follows the hindered-rotor treatment of Pitzer and Gwinn [12].

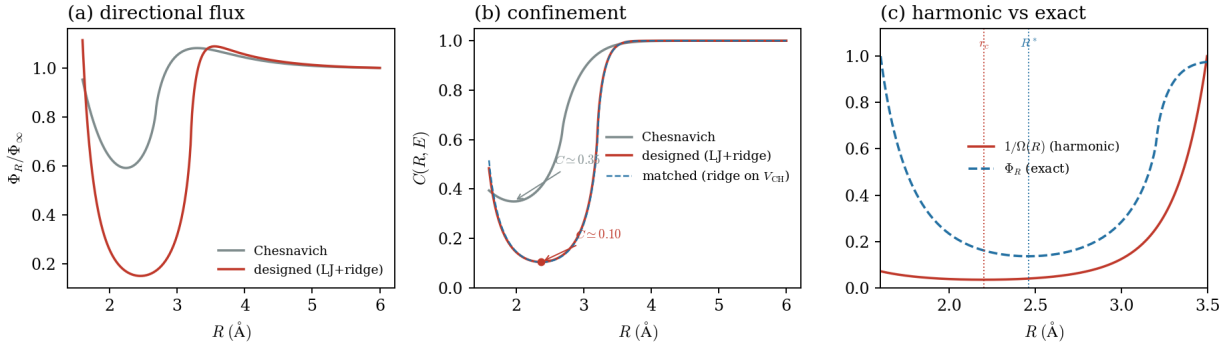


Figure 3: The variational flux bottleneck at $E = 2$. (a) Exact directional flux Φ_R/Φ_∞ , Eq. (11), for the designed (LJ+ridge) and Chesnavich surfaces; the designed model has a deep, narrow minimum where the Chesnavich surface has only a shallow one. (b) Angular confinement $C(R, E)$, Eq. (12): the designed constriction ($C \simeq 0.10$) is reproduced by the matched control (ridge on the Chesnavich channel, dashed), well below the Chesnavich value ($C \simeq 0.35$). (c) Decomposition of the designed-model flux: the harmonic approximation $1/\Omega$ is minimized at $r_c = 2.20$ Å, but the exact flux minimum sits at $r^* = 2.46$ Å because the available channel energy $\varepsilon(R)/\Omega$ shifts it outward.

Figure 3 reports these quantities at $E = 2$. The designed model has a deep, narrow flux minimum at $r^* \simeq 2.46$ Å (designed channel), with $\Phi_{R^*}/\Phi_\infty \simeq 0.15$ and confinement $C \simeq 0.10$: a deep entropic bottleneck on an otherwise barrierless channel, in the sense that only about a tenth of the free transverse phase space still crosses ($C \simeq 0.10$). The Chesnavich surface, by contrast, has only a shallow interior minimum at $r^* \simeq 2.24$ Å with $C \simeq 0.35$, confirming the point of Sec. 2 that the Chesnavich channel *does* possess an entropic bottleneck, but a weak one. The matched control at the level of the flux (the ridge placed on the Chesnavich channel $V_{\text{CH}}(r)$) reproduces the deep constriction almost exactly ($r^* \simeq 2.47$ Å, $C \simeq 0.10$; dashed curve in Fig. 3b), demonstrating that the deep statistical bottleneck is produced by the designed transverse stiffness and transfers between radial channels. The same designed transverse stiffness produces both this deep flux minimum and the dynamical gating of Sec. 4, at their respective radii.

Two features deserve emphasis. First, the flux minimum is genuinely entropic: there is no radial potential barrier along the channel (Fig. 1a), so the constriction is entirely an effect of angular confinement, the reduction of the accessible transverse phase space to $C \simeq 0.10$, not of any radial potential barrier. Second, the flux minimum $r^* \simeq 2.46$ Å does *not* coincide with the maximum of the designed transverse stiffness at $r_c = 2.20$ Å; it sits a little outside it. The decomposition in Fig. 3c shows why: the harmonic approximation $1/\Omega(R)$ is minimized at r_c , but the exact flux carries the additional factor of available channel energy $\varepsilon(R)$, which rises with R along the attractive channel and shifts the true minimum outward. The surface that actually constricts the flux is therefore this radius, a little outside the stiffness maximum.

6 The dynamical transition-state structure

The designed model's three transition states are all unstable periodic orbits, located at $E = 2$ and shown in Fig. 4: the tight orbit at $r^* \simeq 2.46$ Å, a libration of $\pm 12^\circ$ about the aligned axis, at the flux-minimum radius of Sec. 5; the free-rotor orbit over 3.5 – 3.7 Å, used to classify roaming in Sec. 7; and the outer orbiting orbit at $r_{\text{OTS}} = 7.48$ Å. This section locates the last of these.

The invariant phase-space object is the outer orbiting transition state that gates escape. The long-range tail supports an orbiting relative equilibrium on the centrifugal barrier of the rotationally

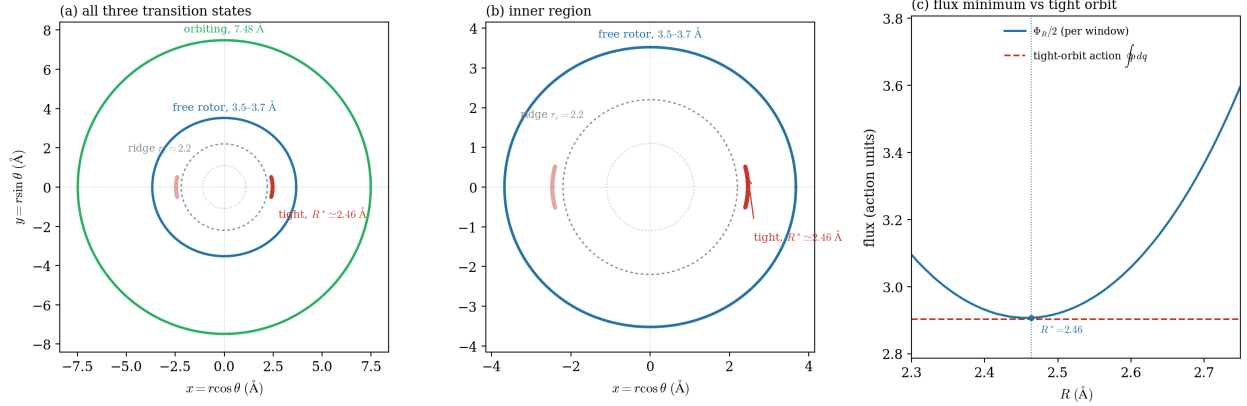


Figure 4: The three transition states of the designed model at $E = 2$, all unstable periodic orbits, in the configuration plane $(x, y) = (r \cos \theta, r \sin \theta)$. (a) All three: the orbiting orbit (circle, $r_{\text{OTS}} = 7.48 \text{ \AA}$), the free-rotor orbit (loop, $r \in [3.5, 3.7] \text{ \AA}$), and the tight orbit (short arc near the aligned axis, $r^* \simeq 2.46 \text{ \AA}$; its $\theta = \pi$ mirror is shown faintly). (b) The inner region: the tight orbit is a libration of $\pm 12^\circ$ about the aligned axis at the flux minimum r^* , where the radial channel is barrierless; the free-rotor orbit is a rotation. The ridge center $r_c = 2.2 \text{ \AA}$ is marked in both panels. (c) The fixed-radius directional flux per aligned window, $\Phi_R/2$, against the action $\oint p dq = 2.902$ of the tight orbit (dashed line): the minimum, 2.907 at R^* , agrees with the orbit’s dividing-surface flux to 0.15% .

averaged effective radial potential $V_{\text{eff}}(r; L) = V_{\text{rad}}(r) + \frac{1}{2}L^2a(r) + \frac{1}{2}B(r)$. Figure 5 shows that at $E = 2$ this potential has a barrier maximum at $r_{\text{OTS}} \simeq 7.48 \text{ \AA}$ with angular momentum $L = p_\theta = 3.047$, the internal rotational momentum (the total angular momentum is zero); the maximum has negative radial curvature, so the orbit is unstable. The full model is not globally rotationally symmetric when $B \neq 0$, so rotational averaging does not in general define an exact orbit; here, however, the ridge is negligible at this radius ($B(r_{\text{OTS}}) \sim 10^{-47}$), so rotational averaging is exact to numerical precision and this is the asymptotic orbiting relative equilibrium. The orbiting transition state is the standard centrifugal (Langevin) barrier, produced by the centrifugal term $\frac{1}{2}L^2a(r)$ against the $-1/r^4$ attraction with no contribution from the ridge. The dividing surface attached to it is defined at this energy and angular momentum ($E = 2$, $L = 3.047$); it is not a fixed radius crossed by every trajectory, since the orbiting-barrier location depends on angular momentum. We do not launch trajectories from this surface: the inward ensemble of Sec. 7 starts at $r_0 = 6 \text{ \AA}$, inside r_{OTS} , and its largest angular momentum equals $L = 3.047$, so the launch grid is bounded in angular momentum by the orbiting transition state while lying radially inside it.

This is the second of the three radii. The dynamical transition state that gates escape, the orbiting orbit at $r_{\text{OTS}} \simeq 7.48 \text{ \AA}$, lies well outside the variational flux bottleneck $r^* \simeq 2.46 \text{ \AA}$. These are different physical objects, an inner entropic constriction and an outer centrifugal escape barrier, so their separation is expected; the substantive point, completed in Sec. 8, is that neither coincides with the classifier, and no single radius summarizes the dynamics.

7 The roaming classifier

Mauguière, Collins, Ezra, Farantos and Wiggins constructed phase-space dividing surfaces from the periodic orbits of the Chesnavich model and classified trajectories by how many times they cross them [22]. Krajňák and Waalkens computed the stable and unstable manifolds of those orbits and described the transport through their lobes [27]; Krajňák and Wiggins obtained the same structures

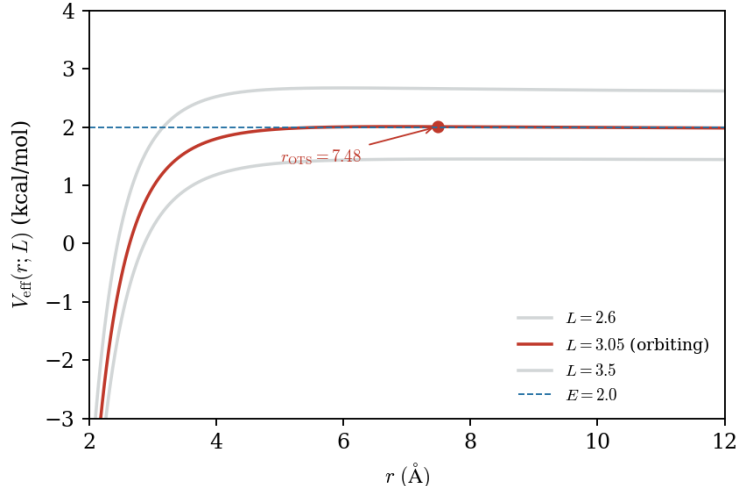


Figure 5: The outer orbiting transition state of the designed model (LJ(8,4) channel). Outer-region effective radial potential $V_{\text{eff}}(r; L)$ at $E = 2$: at $L = 3.047$ the orbiting transition state is the unstable centrifugal barrier maximum at $r_{\text{OTS}} = 7.48$ Å. The ridge is negligible in this region, so the orbiting transition state is the standard centrifugal (Langevin) barrier.

with Lagrangian descriptors, computationally simpler than the manifold construction [28]. We adopt their distinction between direct and roaming trajectories. In the phase-space picture the surface that draws this distinction is the free-rotor periodic-orbit dividing surface; in the designed model at $E = 2$ this is a genuine hyperbolic orbit, a rotational orbit oscillating radially over $r \in [3.52, 3.68]$ Å, and we count crossings of a surface of fixed radius $r_{\text{class}} = 3.5$ Å, at its inner turning point, as a practical stand-in.

For the classifier analysis below we use the LJ(8,4) radial channel, for which the inner-capture fractions quoted in Sec. 4 are 57.3% and 15.1%. We integrate the inward ensemble of Sec. 4, here on this channel, and classify each trajectory two ways. A trajectory is *reactive* if its closest approach reaches the well ($r < 1.6$ Å) and *nonreactive* otherwise; it is *roaming* if it crosses r_{class} three or more times, in either direction, before escaping, and *direct* otherwise. This differs from the original scheme in one respect: there the crossing count alone carries both roaming and reactivity, through the opposite crossing parity of trajectories ending inside versus outside; we read reactivity directly from the closest approach and use a single crossing threshold for roaming. The four combinations are direct-reactive, direct-nonreactive, roaming-reactive, and roaming-nonreactive. Trajectories are integrated to escape or to the time limit, and are not stopped at the well; the two roaming classes therefore come from the same calculation.

Passing both angular interactions through this classifier on the same radial channel isolates what the ridge does. Under the ridge the ensemble divides into 14.9% direct-reactive, 78.9% direct-nonreactive, 6.0% roaming-nonreactive, and 0.13% roaming-reactive; under the lock, into 55.7%, 36.8%, 6.0%, and 1.6%. The total reactive fraction, 57.3% for the lock and 15.1% for the ridge, reproduces the LJ-channel inner-capture numbers quoted in Sec. 4, since reaching the well is the event scored there; the classifier and the capture partition are two readings of one calculation. The roaming fraction is comparable between the two models (7.6% for the lock, 6.2% for the ridge at 3.5 Å), but its radial location is not: under the lock roaming already appears at smaller radii (1.6% at 2.5 Å, rising to 7.6% by 3.0 Å), whereas under the ridge it is negligible inside 3.0 Å (below 0.2%) and switches on sharply near 3.5 Å (Fig. 2b). The ridge does not suppress roaming; it displaces it

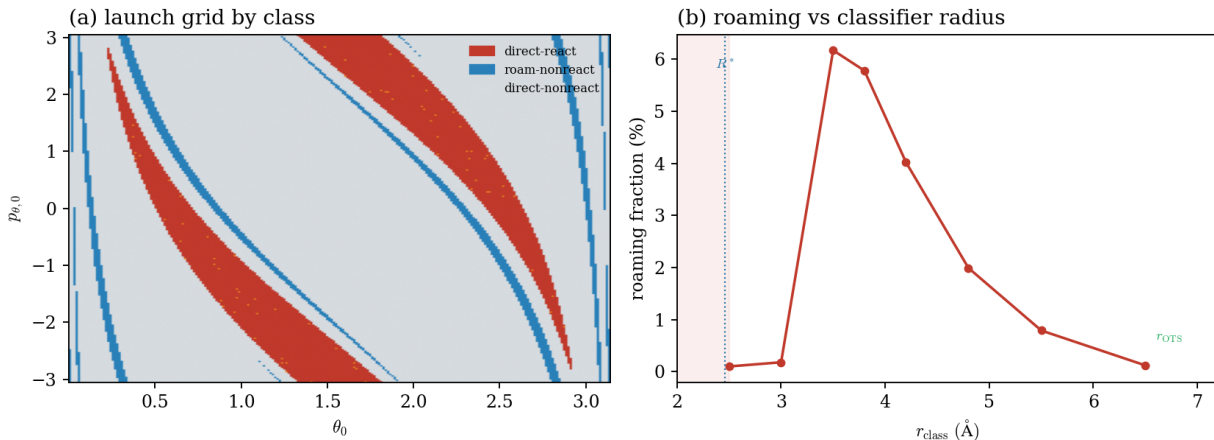


Figure 6: Roaming on the designed surface at $E = 2$ (LJ(8,4) channel; 240×240 inward grid at $r_0 = 6 \text{ \AA}$). (a) Launch grid $(\theta_0, p_{\theta,0})$ colored by trajectory class: reactive trajectories form centrifugal-trapping bands, roaming sets are thin, and most trajectories are direct and nonreactive. The classification is that of the non-absorbing run, in which a small roaming-reactive class appears. (b) Roaming fraction versus classifier radius r_{class} : suppressed inside the ridge (shaded), switching on near 3.5 \AA , and decaying toward zero past the orbiting radius $r_{\text{OTS}} = 7.48 \text{ \AA}$. The flux minimum $r^* = 2.46 \text{ \AA}$ and the orbiting radius are marked; the classifier radius is where this statistic is maximal, not a periodic-orbit dividing surface.

outward, to just beyond the stiffness maximum.

Whether the intermediate dynamics is statistical is tested by the gap time, the residence time between entering and leaving the interaction region: a statistical (Rice–Ramsperger–Kassel–Marcus, RRKM) population decays as a single exponential, so any departure from one shows that a single rate through the bottleneck does not capture the dynamics. The distribution is non-exponential for both the lock and the ridge (Appendix B), consistent with the nonstatistical roaming region found by Mauguière, Collins, Ezra, Farantos and Wiggins [22, 15, 16].

The classifier radius is not sharply determined: the roaming fraction against r_{class} has a broad maximum near $3.4\text{--}3.5 \text{ \AA}$, so radii across that range classify almost identically, and we take 3.5 \AA as representative. Figure 6b shows the corresponding LJ(8,4)-channel roaming fraction over the full radial range, together with the flux minimum r^* , the ridge region, and the orbiting radius r_{OTS} , to place the classifier radius among the transition-state radii. Figure 6a shows the launch grid colored by class. The reactive trajectories fall into bands, centrifugal-trapping bands separated by thin roaming sets, whose arrangement can be fractal [33]. A separate inner feature near 2 \AA comes from trajectories oscillating in the inner region, inside the ridge but above 1.6 \AA , so never reaching the well, and is not outer roaming. Toward large radius the roaming fraction dies out as trajectories escape past the orbiting orbit at $r_{\text{OTS}} = 7.48 \text{ \AA}$.

8 The tight transition state

The designed model carries analogues of the three transition states that organize the Chesnavich model, all of them unstable periodic orbits located here at $E = 2$: the tight orbit at $r \simeq 2.46 \text{ \AA}$, the free-rotor orbit spanning $3.52\text{--}3.68 \text{ \AA}$, and the orbiting orbit at $r_{\text{OTS}} = 7.48 \text{ \AA}$, introduced in Sec. 1. The tight orbit gates entry to the well and is the tight transition state of the original model, present here in the same kind: a hindered-rotor orbit librating within $\pm 12^\circ$ of the aligned axis (Fig. 4). Chesnavich’s original study concerned exactly the competition among such transition

states; here we ask what has changed about the innermost one.

Both models place the tight transition state at a flux minimum where the radial channel is barrierless: the crossing is constricted not by a potential maximum along r but because angular hindrance narrows the accessible transverse phase space. In this sense the tight transition state is entropic in the Chesnavich model as much as in the designed model, and Chesnavich’s transition-state switching is a competition between entropic bottlenecks, neither anchored to a potential saddle. The flux-minimizing dividing surface is moreover the surface spanned by the tight periodic orbit, since the minimum-flux dividing surface is bounded by an unstable periodic orbit [13]: the variational bottleneck $r^* \simeq 2.46 \text{ \AA}$ of Sec. 5 sits at the tight orbit. We verify this directly rather than assume it: in two degrees of freedom the flux through the dividing surface spanned by a periodic orbit equals the orbit’s action $\oint p dq$ [13, 19]; for the numerically located tight orbit this action is 2.902, and the fixed-radius flux minimum per aligned window is $\Phi_{R^*}/2 = 2.907$, an agreement of 0.15% (Fig. 4c; the factor of two counts the two aligned windows $\theta = 0, \pi$, each spanned by one tight orbit). The fixed-radius family thus attains the periodic-orbit flux, and the identification of the variational bottleneck with the tight orbit’s dividing surface is a computed result, not an assumption. What the designed model changes is the depth and location of this entropic bottleneck. The interior maximum of Ω places a deep constriction at an interior radius ($r^* \simeq 2.46 \text{ \AA}$, $C \simeq 0.10$), where the monotone stiffness of the Chesnavich lock, largest at the inner edge and falling outward, gives only a shallow one ($C \simeq 0.35$, Sec. 5). It is this deep, interior entropic bottleneck, not the entropic character as such, that gates inner capture and displaces roaming outward (Secs. 4, 7).

A statistical rate theory would place the bottleneck at r^* and compute a rate through it. But the tight transition state gates only entry; the trajectories it admits do not settle into a single complex, they roam, sorted by the free-rotor surface and released past the orbiting surface, with non-exponential gap-time distributions (Sec. 7). The entropic bottleneck locates where capture is controlled; it does not by itself describe the roaming and escape that follow. That the controlling bottleneck is entropic rather than energetic is the point of contact with Makarov.

Relation to Makarov. Makarov [9] considered a reaction coordinate crossing a region where a transverse mode stiffens, with no potential barrier along the coordinate; integrating out the transverse mode yields a free-energy barrier $G(x) = V(x) + k_B T \ln[\omega_\perp(x)/\omega_0]$ located at the stiffness maximum, a purely entropic barrier. Our fixed-energy $\Omega(r)$ is the microcanonical counterpart of his $\omega_\perp(x)$, and Eq. (1) is the same relation. Makarov further observed that at such a barrier different observables need not agree: the reaction rate is well described by transition-state theory while the distribution of transition-path times is not, because the slow transverse mode carries dynamics that a single rate does not capture. In his model the entropic maximum, the geometric constriction, and the rate-controlling surface all sit at one location. Here the tight transition state is likewise entropic, but it is one of several transition states at separated radii, and the roaming it admits is the nonstatistical dynamics that a rate through it does not describe: a Hamiltonian roaming realization of the same rate-versus-dynamics distinction.

9 Conclusions

We constructed a designed Chesnavich-type roaming model in which the orientation-locking angular hindrance is replaced by a localized maximum of the transverse frequency, a transverse-stiffness ridge on an otherwise barrierless channel, and compared two fixed-energy trajectory ensembles that differ only in the angular interaction, the Chesnavich lock in one and the entropic ridge in the other, with the same radial channel, energy, and inward initial conditions. The central result is

dynamical: with the same radial channel, energy, and inward fixed-energy ensemble, the entropic ridge gates entry into the inner well and converts most of the incoming flux into direct nonreactive return; it does not increase the roaming fraction at the classifier radius but spatially reorganizes it, suppressing it inside the ridge and displacing it outward relative to the Chesnavich lock. Inner-well capture falls from 57.3% to 14.7% and direct nonreactive return rises from 37.4% to 80.3%, while the nonreactive roaming fraction at 3.5 Å is essentially unchanged (5.3% \rightarrow 4.9%) but is pushed outward in radius. The gating is robust across the Chesnavich switching parameter α , and is essentially unchanged when the Chesnavich radial potential is replaced by an LJ(8,4) channel with the same $-1/r^4$ tail; the outward displacement is established for the $\alpha = 1$ comparison. Strength-matched monotone controls separate amplitude from localization: capture tracks the hindrance strength at the bottleneck radius, and a monotone lock matched to the ridge there reproduces both the gating (17.8% capture) and the outward displacement, while at equal global peak amplitude the ridge gates far more effectively than a monotone profile (14.7% against 33.0%). The interior maximum supplies placement, concentrating the hindrance strength at the gating radius.

The phase-space explanation is the set of unstable periodic orbits and their dividing surfaces that control capture and roaming: the tight orbit that gates the well, the free-rotor orbit that sorts direct from roaming, and the orbiting orbit that gates escape, at $r^* \simeq 2.46$ Å, $r_{\text{class}} \simeq 3.5$ Å, and $r_{\text{OTS}} \simeq 7.48$ Å. The variational flux minimum is not a separate statistical surface; it is the dividing surface spanned by the tight periodic orbit, the orbit that gates entry to the well. In one sentence: a localized interior maximum of the transverse stiffness reshapes roaming, gating inner capture and displacing roaming outward, by placing a deep entropic bottleneck at an interior radius. That bottleneck is the tight transition state, an unstable periodic orbit whose dividing surface is the variational minimum-flux surface, barrierless along the reaction coordinate. Its entropic character it shares with the Chesnavich tight transition state; what the interior maximum supplies is the concentration of hindrance strength at the gating radius that makes it control capture. The mechanism is the angular analogue of Makarov’s transverse-stiffening entropic barrier, here placed in a roaming Hamiltonian with a long-range tail and an outer centrifugal transition state, and the roaming it admits is nonstatistical.

A Computational methods

Trajectory ensemble. Trajectories of Eq. (6) are integrated with a fixed-step fourth-order Runge–Kutta (RK4) scheme ($\Delta t = 0.005$ in model time units, $\tau = 0.0489$ ps per unit) at $E = 2$ kcal/mol. The fixed-energy ensemble is a 240×240 grid in $(\theta_0, p_{\theta,0})$ launched inward from $r_0 = 6$ Å. At each grid point the inward radial momentum is fixed by the energy constraint,

$$p_r = -\sqrt{2\mu[E - V_{\text{rad}}(r_0) - \frac{1}{2}B(r_0)(1 - \cos 2\theta_0) - \frac{1}{2}a(r_0)p_{\theta,0}^2]},$$

and grid points for which the radicand is non-positive (energetically inaccessible) are removed; reported fractions are over the energetically accessible set. A trajectory is integrated until it escapes, crossing $r = 8$ Å outward, or reaches the time limit $t_{\text{max}} = 320$ model units (≈ 15.6 ps).

The meaning of “reactive.” Trajectories are not stopped at the inner boundary. Each is integrated until it escapes (crosses $r = 8$ Å outward) or reaches the time limit $t_{\text{max}} = 320$ model units, and its closest approach r_{min} and its crossings of $r = 3.5$ Å are recorded along the way. A trajectory is *reactive* if $r_{\text{min}} < 1.6$ Å, that is, if it enters the well, and *roaming* if it crosses $r = 3.5$ Å three or more times in either direction. Because capture is registered by the closest approach, the

inner-capture fractions of Sec. 4 do not depend on whether integration is continued past the well: stopping there would affect only trajectories that enter and later re-emerge. Continuing resolves that small class (0.13% of trajectories enter the well, cross back outward, and roam, the roaming-reactive class, alongside the 6.04% that roam without entering) and both come from the same run. “Reactive” therefore denotes entry into the well, not committed product formation: the flow is volume-preserving and a captured trajectory may in principle redissociate.

Switching-parameter dependence. The Chesnavich lock width α controls how early the angular hindrance switches off. The comparisons of Sec. 4 use the standard value $\alpha = 1$; the early-switching case $\alpha = 4$ is reported there to show that the roaming fraction is parameter-dependent while the inner-well gating is not; the outward redistribution is demonstrated explicitly only for the $\alpha = 1$ classifier-radius sweep.

Exact directional flux. The flux Eq. (11) and confinement Eq. (12) are evaluated by adaptive quadrature in θ on a dense grid in R ; the integrand’s positive-part support is resolved by refining near the turning angles. The reported minima are stable to grid refinement at the ~ 0.01 Å level, which is the resolution to which r^* is quoted.

Outer boundary. Capture and classifier statistics use an outer removal radius $r = 8$ Å; the orbiting transition state and the effective-potential construction of Sec. 6 were checked against an extended boundary $r = 12$ Å, with no change to r_{OTS} or to the reported fractions beyond the last quoted digit.

Numerical validation. The reported fractions are converged in grid, step, and integration time. On the Chesnavich channel the inner-capture fractions move from 57.11%/14.68% (lock/ridge) on a 120×120 launch grid to 57.27%/14.75% on the 240×240 production grid, a shift below 0.1 percentage points; the capture fraction is identical to two decimals at $\Delta t = 0.01, 0.005,$ and 0.0025 . The fixed-step RK4 integrator conserves energy to $|H - E| \lesssim 2 \times 10^{-7}$ kcal/mol over complete trajectories, and at $t_{\text{max}} = 320$ model units (≈ 15.6 ps) only 0.085% of trajectories (49 of 57,600) remain unclassified inside the interaction region.

Tight-orbit dividing-surface flux. The tight periodic orbit is located by a Newton search on the $\sin \theta = 0$ surface of section (converged initial condition $(r, p_r, \theta, p_\theta) = (2.4689, 0, 0, 4.3505)$, period $T = 0.5134$ at $E = 2$). The flux through the dividing surface it spans equals its action $\oint p dq$, accumulated along one period by RK4 at $\Delta t = T/1.2 \times 10^5$; the orbit closes to $|y(T) - y(0)| < 10^{-4}$ with $|H - E| \leq 10^{-4}$ along it. The resulting action, 2.902, agrees with the per-window fixed-radius flux minimum $\Phi_{R^*}/2 = 2.907$ to 0.15% (Fig. 4c).

B Gap-time analysis

The *gap time* of a trajectory is the residence time between one inward crossing of the launch surface $r_0 = 6$ Å and the next outward crossing. Its distribution is a classical diagnostic of statistical versus nonstatistical decay: in the statistical (RRKM) picture escape is memoryless, and the survival function $S(t)$, the fraction of the entering ensemble still inside at time t , is a single exponential set by one rate-limiting bottleneck. A departure from a single exponential indicates that the escape is not memoryless: the residence times carry structure that a single rate does not capture, either a tail heavier than exponential (trapping and recrossing) or a short-time shoulder with a lighter

tail (fast, direct transits on a characteristic crossing time). The gap-time formulation is due to Thiele [15], following Slater’s dynamical theory of unimolecular reactions [34, 35], and was cast in the phase-space transition-state setting by Ezra, Waalkens and Wiggins [16]; Mauguière, Collins, Ezra, Farantos and Wiggins applied it to the roaming region of the Chesnavich model and likewise found nonstatistical behavior [22].

The criterion deserves emphasis. Statisticality is a hypothesis about dynamics—memoryless escape at a single rate—and the gap-time distribution tests it directly on the trajectories themselves. Nonstatisticality in roaming is sometimes framed instead in terms of ergodic exploration of the long-range region [5]; but the energy shell here is unbounded and trajectories escape through the radical channel, so ergodicity in its standard sense is not defined for this flow, whereas the gap-time test is constructed for precisely such open systems.

We compute $S(t)$ on the same fixed-energy ensemble used throughout, the 240×240 inward grid launched from $r_0 = 6 \text{ \AA}$ (Appendix A), so that the diagnostic describes the very trajectories whose capture and roaming Secs. 4 and 7 characterize, not a separately launched set. For each nonreactive trajectory we record the time from its inward launch at $r_0 = 6 \text{ \AA}$ until it escapes, crossing $r = 8 \text{ \AA}$ outward. Because $r_0 = 6 \text{ \AA}$ lies inside the orbiting transition state ($r_{\text{OTS}} \simeq 7.48 \text{ \AA}$), these are conditional-on-entry residence times, not full collision lifetimes; the non-exponential character found below holds for other launch surfaces as well, so $r_0 = 6 \text{ \AA}$ is fixed by consistency with the rest of the paper rather than to obtain the result. Two caveats on the construction itself. Conditioning on the nonreactive outcome means this is not the gap-time distribution of the complete incoming flux through a dividing surface; it is the conditional distribution of nonreactive return times, and it is that distribution we test. And part of the short-time behavior is deterministic: no trajectory can exit before the minimum transit time from r_0 in and back out, so the flat shoulder at small t is guaranteed, and the informative comparison with an exponential is the shape of the decay beyond that direct-transit interval.

Figure 7a shows $S(t)$ for the Chesnavich lock and the entropic ridge, each with the matched single exponential overlaid. Both are manifestly non-exponential and *narrower* than exponential: coefficient of variation (CV, the ratio of standard deviation to mean) 0.68 for the lock and 0.75 for the ridge, against 1 for a memoryless decay, with tails lighter than exponential beyond the transit shoulder. Figure 7b resolves the ridge ensemble into its direct and roaming-classified components, and this is the sharper statement. The two populations are well separated—mean return times 0.257 ps (direct) and 0.878 ps (roaming)—and each is itself narrow (CV 0.45 and 0.49); the lock decomposes the same way (0.302 and 0.775 ps, CV 0.44 and 0.49). The full distribution is therefore a bimodal mixture of fast direct returns and slower roaming returns, not a memoryless decay at any single rate. In particular the roaming-classified subset—the population whose statisticality is at issue—has return times tightly clustered about a characteristic value where a statistical (RRKM) escape would give $\text{CV} = 1$ and an exponential tail: the roaming is nonstatistical in the direct sense that its residence times are inconsistent with memoryless single-rate escape. The entropic bottleneck sets how much enters, not the pace of what crosses: the transit-time-versus-rate decoupling Makarov identifies for an entropic barrier. The mean nonreactive gap times over the full ensembles are 0.368 ps (lock) and 0.301 ps (ridge).

Data availability

This study reports no experimental data. All results were generated by trajectory integration of the classical Hamiltonian models defined in Sections 2 and 3, with the parameters of Table 1 and the integrator of Appendix A. The scripts that reproduce every figure and reported quantity are

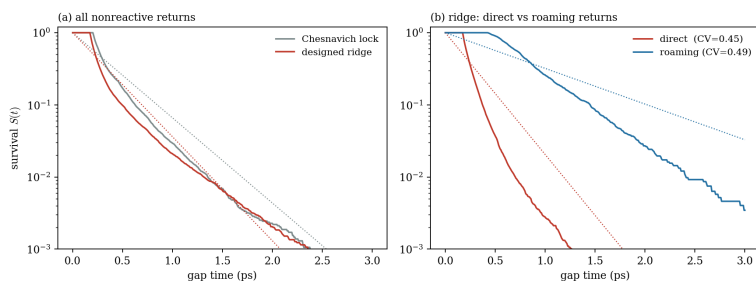


Figure 7: Nonreactive gap-time survival ($r_0 = 6 \text{ \AA}$ launch, conditional on inward entry). (a) Chesnavich lock and entropic ridge; dotted curves are matched single exponentials. Both distributions are narrower than exponential, with a delayed onset set by the minimum transit time. (b) The ridge ensemble resolved into direct and roaming-classified returns: the two populations are individually narrow (coefficient of variation $CV = 0.45$ and 0.49) and well separated in time; the full distribution is their bimodal mixture, inconsistent with memoryless single-rate decay.

available from the author upon reasonable request.

References

- [1] D. Townsend, S. A. Lahankar, S. K. Lee, S. D. Chambreau, A. G. Suits, X. Zhang, J. Rheinecker, L. B. Harding, and J. M. Bowman, *The roaming atom: straying from the reaction path in formaldehyde decomposition*, *Science* **306**, 1158–1161 (2004).
- [2] A. G. Suits, *Roaming atoms and radicals: a new mechanism in molecular dissociation*, *Acc. Chem. Res.* **41**, 873–881 (2008).
- [3] J. M. Bowman, *Roaming*, *Mol. Phys.* **112**, 2516–2528 (2014).
- [4] J. M. Bowman and B. C. Shepler, *Roaming radicals*, *Annu. Rev. Phys. Chem.* **62**, 531–553 (2011).
- [5] A. G. Suits, *Roaming reactions and dynamics in the van der Waals region*, *Annu. Rev. Phys. Chem.* **71**, 77–100 (2020).
- [6] R. Fernando, A. Dey, B. M. Broderick, B. Fu, Z. Homayoon, J. M. Bowman, and A. G. Suits, *Visible/infrared dissociation of NO_3 : roaming in the dark or roaming on the ground?*, *J. Phys. Chem. A* **119**, 7163–7168 (2015).
- [7] D. J. Tantillo, *Beyond transition state theory—non-statistical dynamic effects for organic reactions*, *Adv. Phys. Org. Chem.* **55**, 1–16 (2021).
- [8] H.-X. Zhou and R. Zwanzig, *A rate process with an entropy barrier*, *J. Chem. Phys.* **94**, 6147–6152 (1991). doi:10.1063/1.460427.
- [9] D. E. Makarov, *Reconciling transition path time and rate measurements in reactions with large entropic barriers*, *J. Chem. Phys.* **146**, 071101 (2017). doi:10.1063/1.4977177.
- [10] Y. Georgievskii and S. J. Klippenstein, *Long-range transition state theory*, *J. Chem. Phys.* **122**, 194103 (2005).
- [11] D. G. Truhlar, B. C. Garrett, and S. J. Klippenstein, *Current status of transition-state theory*, *J. Phys. Chem.* **100**, 12771–12800 (1996).
- [12] K. S. Pitzer and W. D. Gwinn, *Energy levels and thermodynamic functions for molecules with internal rotation. I. Rigid frame with attached tops*, *J. Chem. Phys.* **10**, 428–440 (1942).

- [13] E. Pollak and P. Pechukas, *Transition states, trapped trajectories, and classical bound states embedded in the continuum*, J. Chem. Phys. **69**, 1218–1226 (1978).
- [14] P. Pechukas and E. Pollak, *Classical transition state theory is exact if the transition state is unique*, J. Chem. Phys. **71**, 2062–2068 (1979).
- [15] E. Thiele, *Comparison of the classical theories of unimolecular reactions*, J. Chem. Phys. **36**, 1466–1472 (1962).
- [16] G. S. Ezra, H. Waalkens, and S. Wiggins, *Microcanonical rates, gap times, and phase space dividing surfaces*, J. Chem. Phys. **130**, 164118 (2009).
- [17] S. Wiggins, *The role of normally hyperbolic invariant manifolds (NHIMs) in the phase-space setting for chemical reaction dynamics*, Regul. Chaotic Dyn. **21**, 621–638 (2016).
- [18] H. Waalkens and S. Wiggins, *Geometrical models of the phase space structures governing reaction dynamics*, Regul. Chaotic Dyn. **15**(1), 1–39 (2010).
- [19] H. Waalkens, R. Schubert, and S. Wiggins, *Wigner’s dynamical transition state theory in phase space: classical and quantum*, Nonlinearity **21**(1), R1–R118 (2008).
- [20] W. J. Chesnavich, *Multiple transition states in unimolecular reactions*, J. Chem. Phys. **84**, 2615 (1986).
- [21] T. Su and W. J. Chesnavich, *Parametrization of the ion–polar molecule collision rate constant by trajectory calculations*, J. Chem. Phys. **76**, 5183 (1982).
- [22] F. A. L. Mauguière, P. Collins, G. S. Ezra, S. C. Farantos, and S. Wiggins, *Roaming dynamics in ion–molecule reactions: phase space reaction pathways and geometrical interpretation*, J. Chem. Phys. **140**, 134112 (2014).
- [23] F. A. L. Mauguière, P. Collins, G. S. Ezra, S. C. Farantos, and S. Wiggins, *Multiple transition states and roaming in ion–molecule reactions: a phase space perspective*, Chem. Phys. Lett. **592**, 282 (2014).
- [24] F. A. L. Mauguière, P. Collins, Z. C. Kramer, B. K. Carpenter, G. S. Ezra, S. C. Farantos, and S. Wiggins, *Phase space structures explain hydrogen atom roaming in formaldehyde decomposition*, J. Phys. Chem. Lett. **6**, 4123–4128 (2015).
- [25] F. A. L. Mauguière, P. Collins, Z. C. Kramer, B. K. Carpenter, G. S. Ezra, S. C. Farantos, and S. Wiggins, *Phase space barriers and dividing surfaces in the absence of critical points of the potential energy: application to roaming in ozone*, J. Chem. Phys. **144**, 054107 (2016).
- [26] F. A. L. Mauguière, P. Collins, Z. C. Kramer, B. K. Carpenter, G. S. Ezra, S. C. Farantos, and S. Wiggins, *Roaming: a phase space perspective*, Annu. Rev. Phys. Chem. **68**, 499–524 (2017).
- [27] V. Krajňák and H. Waalkens, *The phase space geometry underlying roaming reaction dynamics*, J. Math. Chem. **56**(8), 2341–2378 (2018). doi:10.1007/s10910-018-0895-4.
- [28] V. Krajňák and S. Wiggins, *Influence of mass and potential energy surface geometry on roaming in Chesnavich’s CH_4^+ model*, J. Chem. Phys. **149**(9), 094109 (2018). doi:10.1063/1.5044532.
- [29] V. Krajňák and S. Wiggins, *Roaming in acetaldehyde*, J. Chem. Phys. **160**, 244104 (2024). doi:10.1063/5.0212443.
- [30] G. S. Ezra and S. Wiggins, *The Chesnavich model for ion–molecule reactions: a rigid body coupled to a particle*, Int. J. Bifurcation Chaos **29**(2), 1950025 (2019). doi:10.1142/S0218127419500251.
- [31] V. Krajňák, G. S. Ezra, and S. Wiggins, *Roaming at constant kinetic energy: Chesnavich’s model and the Hamiltonian isokinetic thermostat*, Regul. Chaotic Dyn. **24**(6), 615–627 (2019). doi:10.1134/S1560354719060030.

- [32] V. Krajňák, G. S. Ezra, and S. Wiggins, *Using Lagrangian descriptors to uncover invariant structures in Chesnavich's isokinetic model with application to roaming*, Int. J. Bifurcation Chaos **30**, 2050076 (2020).
- [33] M. E. Grice, B. K. Andrews, and W. J. Chesnavich, *A threshold study of the classical dynamics of collision-induced dissociation in collinear H + H₂*, J. Chem. Phys. **87**, 959–968 (1987).
- [34] N. B. Slater, *New formulation of gaseous unimolecular dissociation rates*, J. Chem. Phys. **24**, 1256 (1956).
- [35] N. B. Slater, *Theory of Unimolecular Reactions* (Cornell University Press, Ithaca, NY, 1959).